Chapter 2 - COMPILATION AND ANALYSIS OF SECOND-MODE AMPLITUDES ON SHARP CONES IN HYPERSONIC WIND TUNNELS

Eric C. Marineau
Arnold Engineering Development Complex
UNITED STATES OF AMERICA

Guillaume Grossir
von Karman Institute for Fluid Dynamics
BELGIUM

Alexander Wagner
German Aerospace Center (DLR)
GERMANY

Madlen Leinemann and Rolf Radespiel
Technische Universität Braunschweig
GERMANY

Hideyuki Tanno
Japan Aerospace Exploration Agency (JAXA)
JAPAN

Tim P. Wadhams
CUBRC
UNITED STATES OF AMERICA

Brandon C. Chynoweth and Steven P. Schneider
Purdue University
UNITED STATES OF AMERICA

Ross M. Wagnild and Katya M. Casper
Sandia National Laboratories
UNITED STATES OF AMERICA

2.0 NOMENCLATURE

A	pressure fluctuation RMS normalized by the mean edge pressure
a	pressure spectral amplitude on cone surface normalized by mean edge pressure, 1/Hz$^{0.5}$
A_0	initial amplitudes of the second-mode normalized by the mean edge pressure
A_{max}	maximum pressure fluctuation RMS of the second-mode normalized by the mean edge pressure
C_R	receptivity coefficient
d_n	nozzle diameter at the exit plane, m

F	dimensionless frequency
f	frequency, Hz
h_n	nozzle height at the exit plane, m
l	constant for freestream noise fit
L_c	cone length, m
L_n	nozzle length, m
M	Mach number
m	slope of the freestream noise power spectral density
N	N factor
p	mean pressure, Pa
R	stability Reynolds number defined as square root of Reynolds number based on freestream quantities and surface coordinate
R_n	nose radius, mm
R_T	stability Reynolds number at start of transition, m
Re/m	freestream unit Reynolds number, 1/m
Re_x	Reynolds number based on freestream condition and surface coordinates
S_T	surface coordinate at start of transition, m
u	velocity, m/s
w	constant for second-mode bandwidth
w_n	nozzle width at the exit plane, m
α	dimensionless second-mode growth rate
δ_n	nozzle wall boundary-layer thickness, m
Γ_0	normalized freestream noise amplitude integrated over the second-mode bandwidth
γ_0	normalized pitot noise spectral amplitude, 1/Hz
Δf	second-mode bandwidth, Hz
ϕ	freestream noise power spectral amplitude, Pa^2/Hz
θ_c	cone half-angle, deg
ρ	density, kg/m^3

Subscripts

e	boundary layer edge conditions
ET	end of transition
T or ST	at start of transition
w	wall conditions
0	stagnation conditions or at neutral point
os	outer scaling
∞	freestream conditions

2.1 INTRODUCTION

Over the last 10 years, second-mode amplitude measurements have been performed in several hypersonic wind tunnels worldwide using fast-response piezoelectric pressure sensors (PCB-132) [1–10]. These measurements can provide quantitative growth rates and breakdown amplitudes of the second-mode instability which dominates the boundary layer transition (BLT) process for hypersonic flows over slender bodies at moderate angles of attack. The same pressure sensors enabled fast pitot-pressure measurements to quantify the freestream noise content at frequencies up to approximately 750 kHz [11–13]. Such high frequency measurements are required to characterize the spectral amplitudes of the freestream noise over the range of unstable second-mode frequencies.

Over the same time period, the development of robust and user-friendly linear stability theory (LST) and parabolized stability equation (PSE) solvers such as STABL and STABL-3D [14] have democratized the access to LST and PSE predictions. Such tools have facilitated fully integrated experimental and computational studies of second-mode dominated hypersonic BLT [5, 10]. These studies have contributed to the development of a new wind-tunnel prediction methodology [15] based on Mack's amplitude method [16]. The method uses linear stability computations, tunnel noise measurement, and experimentally determined correlations for the second-mode breakdown amplitudes and receptivity coefficients to predict the start of BLT. The new methodology allows a more efficient use of conventional (noisy) wind tunnels to characterize BLT on hypersonic vehicles. This is key, as current quiet wind tunnels only operate at Mach 6, moderate Reynolds numbers, and low enthalpies. These limitations mean that conventional wind tunnels must be used for the test and evaluation of hypersonic vehicles.

The main objectives of this current international research effort undertaken by the North Atlantic Treaty Organization (NATO) Science and Technology Organization (STO) Applied Vehicle Technology (AVT)-240 specialists' group was to compile and analyze second-mode amplitudes measured on sharp slender cones at 0 deg angle of attack (AOA). For the most part, the study involves the reanalysis and interpretation of existing datasets from 11 hypersonic wind tunnels from 3 NATO countries (Belgium, Germany, and USA) and Japan that provide second-mode amplitudes at Mach numbers M between 5 and 14, unit Reynolds numbers Re/m between 1.5 and 16×10^6/m per meter, and wall-to-total temperature ratios T_w/T_0 between 0.1 and 0.8. This wide range of key parameters and tunnel sizes makes it possible to evaluate their effect on the second-mode growth rates, initial amplitudes (A_0) and maximum amplitudes (A_{max}) near the onset of BLT.

This chapter is organized as follows. Section 2.2 describes the experimental facilities, test conditions, test articles, and pressure instrumentation. Section 2.3 presents the computational methodology and discusses the scaling of sharp cone stability and the effect of the Mach number and wall temperature ratio. Section 2.4 compiles the second-mode amplitude measurements and introduces the methodology used to compare the measurements to PSE. Section 2.5 explores the effect of Re/m on the initial amplitudes and correlate the amplitudes. The chapter concludes by summarizing the main findings and providing an overview of future research.

2.2 EXPERIMENTAL METHOD

2.2.1 Experimental Facilities and Test Conditions

The current study uses BLT data collected in 11 ground test facilities operated by 9 organizations located in 4 countries. The facilities are the Sandia National Laboratories (SNL) Hypersonic Wind Tunnel [17] with its interchangeable Mach 5, 8, and 14 nozzles (HWT-5, HWT-8 and HWT-14); the Purdue University Boeing/AFOSR Mach-6 Quiet Tunnel (BAM6QT) [18]; the NASA Langley Research Center 15-Inch Mach 6 Wind Tunnel (15inM6), 20-Inch Mach 6 Wind Tunnel (20inM6), and 31-Inch Mach 10 Wind Tunnel (31inM10) [19]; the Technical University Braunschweig (TUB) Mach 6 Hypersonic Ludwieg Tube Braunschweig (HLB) [20]; the German Aerospace Center (DLR) High Enthalpy Shock-tunnel Göttingen (HEG) [21] with its Mach 8 nozzle; the Japan Aerospace Exploration Agency (JAXA) High Enthalpy Shock Tunnel (HIEST) [22] with its Mach 8 nozzle; The von Karman Institute for Fluid Dynamics (VKI) Longshot hypersonic wind-tunnel [23] with its Mach 10 nozzle, the CUBRC Large Energy National Shock Tunnel I (LENS I) [24, 25] with its Mach 10 nozzle; and the Arnold Engineering Development Complex (AEDC) Hypervelocity Wind Tunnel 9 (T9) [26, 27] with its interchangeable Mach 10 and 14 nozzles. The CUBRC data were not included in this chapter since they were being collected and processed at the time of writing. These data will be included in a future publication.

The facility characteristics and dimensions are listed in Table 2-1. The list includes eight blowdown tunnels, three shock tunnels, two Ludwieg tubes, and one gun tunnel. The overall range of Mach numbers and unit Reynolds numbers are between 5-14 and 1.5-16$\times 10^6$/m, respectively. It is important to note that the unit Reynolds numbers and Mach numbers listed in Table 2-1 do not represent the entire operational envelope of each facility, but strictly covers the range of conditions pertaining to the BLT data analyzed in this chapter. The flow is expanded through contoured axisymmetric nozzles with the exception of the NASA 20inM6 and 31inM10 with two-dimensional nozzles. The nozzle exit diameters vary from 0.24 m for the Purdue BAM6QT to 1.52 m for AEDC T9. The relative scales of the nozzles are shown in Figure 2-1 where the facilities are arranged by increasing Mach numbers and nozzle exit dimensions. All the facilities have conventional (noisy) freestreams with the exception of the BAM6QT that generates a quiet freestream by maintaining a laminar boundary-layer on its highly polished nozzle wall. The BAM6QT can also produce a noisy freestream by closing the bleed-valve located upstream of the nozzle throat [18].

2.2.2 Test Articles and Instrumentation

BLT measurements have been performed on 7-deg half-angle cones in each of the tunnels listed in the previous section. To promote transition under quiet flow, the BAM6QT experiments were also performed on a flared cone

Table 2-1: Description Of Ground Test Facilities Geometries And Cone Test Articles.

Name	Organization	Operation	Geometry	M_∞	Re/m, 1/m x 10^{-6}	d_n or $h_n \times w_n$, m	Θ_c, deg	R_n, mm	L_c, m
HWT-5	SNL	Blowdown	Axisymmetric	*5*	10 - 12.8	0.46	7	0.03	0.52
BAM6QT	Purdue	Ludwieg tube	Axisymmetric	*6*	6.4 - 12	0.24	2.5, 3, 7 & flared	0.03	0.52
15inM6	NASA	Blowdown	Axisymmetric	*6*	6.7	0.38	7	0.03	0.52
HLB	TUB	Ludwieg tube	Axisymmetric	*6*	5.0 - 16	0.50	7	0.09	0.50
20inM6	NASA	Blowdown	2D	*6*	6.8 - 13	0.51 x 0.51	7	0.03	0.51
HWT-8	SNL	Blowdown	Axisymmetric	*8*	4.1 - 13	0.36	7	0.03	0.52
HEG	DLR	Shock tunnel	Axisymmetric	*8*	1.5 - 2.4	0.59	7	2.5	1.10
HIEST	JAXA	Shock tunnel	Axisymmetric	*8*	3.3 - 4.8	0.80	7	2.5	1.00
Longshot	VKI	Gun tunnel	Axisymmetric	*10*	3.3 - 12	0.43	7	0.2	0.80
31inM10	NASA	Blowdown	2D	*10*	1.7 - 6.6	0.79 x 0.79	7	0.03	0.52
LENS I	CUBRC	Shock Tunnel	Axisymmetric	*10*	2.0 - 15	1.22	7	0.15	2.44
Tunnel 9	AEDC	Blowdown	Axisymmetric	*10*	2.0 - 15	1.52	7	0.15	1.55
HWT-14	SNL	Blowdown	Axisymmetric	*14*	3.3	0.46	7	0.03	0.52
Tunnel 9	AEDC	Blowdown	Axisymmetric	*14*	1.7 - 12	1.52	7	0.15	1.55

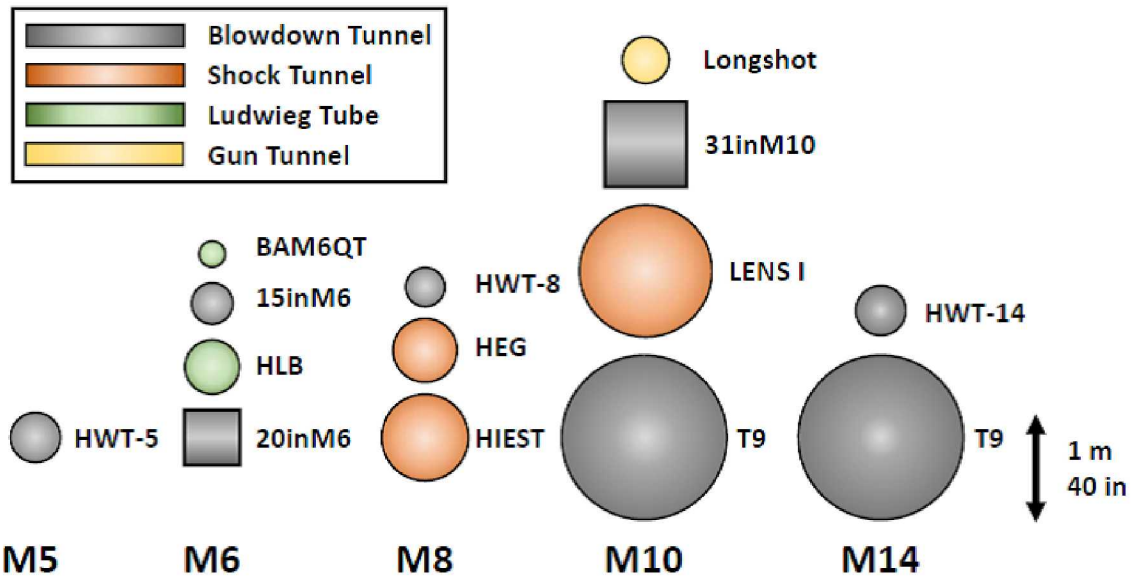

Figure 2-1: Depiction Of Ground Test Facilities Geometries And Dimensions Of The Nozzle Exit Plane.

to destabilize the second-mode as well as on 2.5 and 3-deg cones. The shallower cones enable longer running lengths compared to 7-deg cones with similar base diameters and tunnel blockage. The characteristics of the test articles are found in the last three columns of Table 2-1. With the exception of the HEG and HIEST experiments with a 2.5 mm nosetip radius, the cones can be considered sharp as the nosetips radii (from 0.03 to 0.2 mm) should be small enough to avoid any significant influence of bluntness on the second-mode growth and receptivity. Recent DNS studies by Balakumar and Chou [28] of the Tunnel 9 Mach 10 sharp cone transition experiments [5] showed that the receptivity coefficients increase only slightly with increasing nosetip Reynolds

numbers. For all the experiments, the amplitude of the pressure fluctuations on the surface of the cone were measured with flush-mounted PCB-132 piezoelectric pressure transducers. These sensors have a resonant frequency above 1 MHz, and a flat frequency response to at least several hundred kilohertz. The number of sensors, sensor locations, and number of instrumented rays varied among the experiments. However, in most cases, the number of sensors and sensor spacing were sufficient to characterize the growth rates and breakdown amplitudes. More details about the test articles, instrumentation, and data acquisition can be found in Casper et al. [9, 29] for the SNL experiments, Berridge et al. [2] and Rufer and Berridge [3] for NASA experiments, Wagner et al. [7] for the HEG experiments, Tanno et al. [8] for the HIEST experiments, Grossir et al. [4] for the VKI experiments, and Marineau et al. [5, 10] for the AEDC experiments.

2.3 COMPUTATIONAL METHOD

2.3.1 Linear Stability Computations

The mean flow for the stability analysis is calculated using a structured, axisymmetric computational fluid dynamic (CFD) solver which is part of the STABL software from Johnson and Candler [14] and solves the reacting Navier-Stokes equations. This flow solver is based on the finite-volume formulation. The inviscid fluxes are based on the modified Steger-Warming flux vector splitting method and are second-order accurate with a monotonic upstream-centered scheme for conservation laws (MUSCL) limiter as the total variation diminishing (TVD) scheme. The viscous fluxes are second-order accurate. The time integration method is the implicit, first-order data parallel line relaxation (DPLR) method. Sutherland's law is used for the viscosity, and the heat conductivity is calculated using Eucken's relation. The mean flow for each case is computed on a single-block, structured grid. Each grid is clustered near the wall and the nose of the test geometry in order to capture the fluid gradients at these locations. The stability analyses are performed using the PSE-Chem solver [14], which is also part of the STABL software suite. PSE-Chem solves the reacting, two-dimensional, axisymmetric, linear parabolized stability equations (PSE) to predict the amplification of disturbances as they interact with the boundary-layer. The PSE-Chem solver includes finite-rate chemistry and translational-vibrational energy exchange.

2.3.2 Scaling of Sharp Cone Stability

The scaling from Stetson et al. [30] was used by Marineau et al. [5] to compare sharp cone stability measurements at different unit Reynolds numbers. For convenience, the dimensionless frequency F is defined using the freestream conditions as

$$F = \frac{2\pi f}{u_\infty Re/m}, \tag{1}$$

where u_∞ is the freestream velocity. For sharp cone data, Marineau [15] has shown that the maximum N factor envelope, computed with PSE, can be expressed as

$$N = \alpha R + b, \tag{2}$$

where α and b are constants and R is the the stability Reynolds number defined as

$$R = \sqrt{Re_x}. \tag{3}$$

The stability Reynolds number at the neutral point is obtained by solving Eq. (2) for R with N=0 which leads to

$$R_0 = \frac{-b}{\alpha}. \tag{4}$$

In addition, the most unstable second-mode frequency, which corresponds to the frequency of the maximum N factors can be expressed as

$$F = \frac{g}{R^h}, \tag{5}$$

where g and h are constants. In practice $h \approx 1$, such that F approximately scales as $1/R$. In cold hypersonic wind tunnels, the variation of the wall-to-total temperature ratio T_w/T_0 at a given nominal Mach number is small, such that the same set of constants (α,b,g and h) can be used to parametrize the PSE solutions. Generally, the total temperature is kept as low as possible to maximize the unit Reynolds number for a given stagnation pressure while avoiding flow condensation. This means that cold flow wind tunnels operating at the same nominal Mach number generally operate at similar T_w/T_0. Scaled PSE solutions for a sharp 7-deg cone in HWT-8 at 3 unit Reynolds number and wall temperature ratios are shown in Figure 2-2 along with the curve-fits based on Eqs. 2 and 5. The unit Reynolds numbers and T_w/T_0 are 3.6, 7.4, and 10×10^6/m and 0.35, 0.48, and 0.48, respectively. The variation in T_w/T_0 among the 3 solutions has a minor effect on the quality of the fit. The only discernible difference is the minor increase of F at the lowest unit Reynolds number solution which is most likely due to the thinner boundary layer at the lower T_w/T_0 compared to the two other solutions.

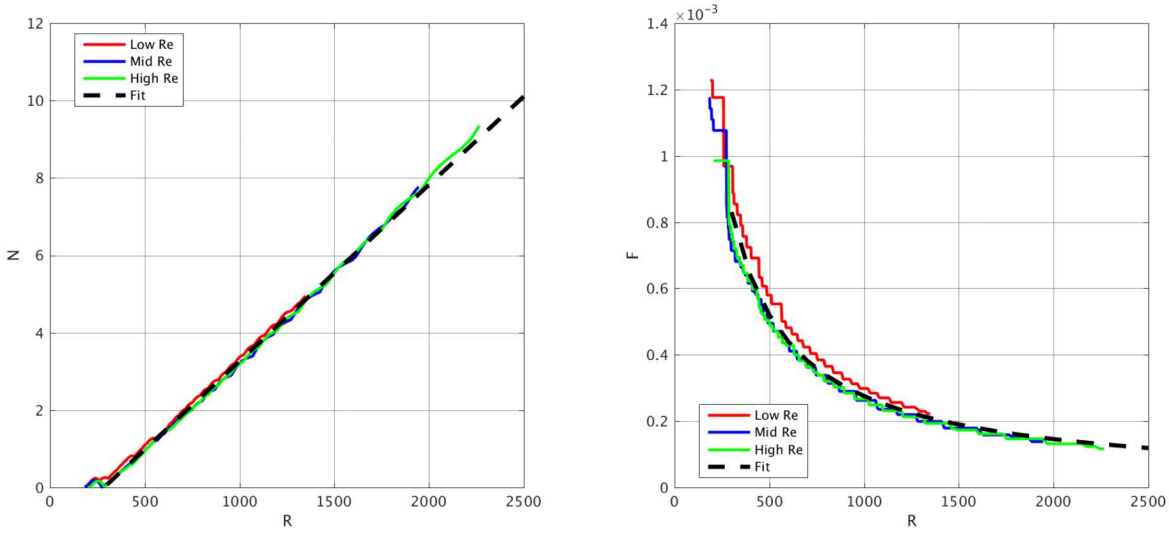

(a) N vs. R (b) F vs. R

Figure 2-2: N vs. R and F vs. R for 3 Re/m and T_0 Conditions in HWT-8.

2.3.3 Effect of Mach Number and Wall Temperature Ratio on Sharp Cone Stability

Linear fits of the PSE solutions for freestream Mach numbers of 5, 6, 8, 10, and 14 are shown in Figure 2-3. In order to prevent flow condensation, the stagnation temperature has to increase with Mach number. This leads to

a decrease of T_w/T_0 from 0.7 at Mach 5 to 0.2 at Mach 14. These conditions are representative of the cold-flow tunnels presented in section 2.2. The curves at Mach 14 correspond to the Tunnel 9 and HWT-14 which operate at different wall-to-total temperature ratios of 0.2 and 0.3 respectively. The Mach number has a strong effect on the growth rate as shown in Figure 2-4a. A strong increase occurs between Mach 5 and Mach 6 followed with a monotonic decrease. These trends are consistent with previous studies from the literature [31, 32]. The variation of the neutral point with Mach number is presented in Figure 2-4b. R_0 decreases from Mach 5 to 10 and increases from Mach 10 to 14. The PSE solutions presented in this section are used to scale the measured amplitude as N factors and to estimate the initial amplitudes in Section 2.4 and 2.5, respectively.

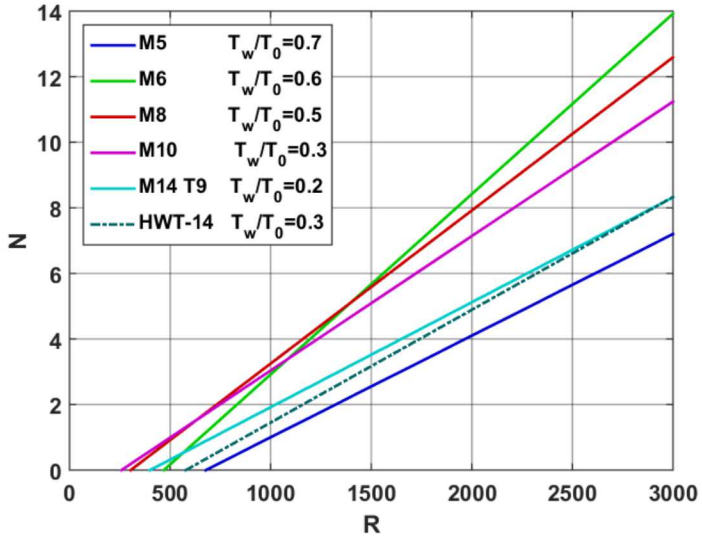

Figure 2-3: N vs. R for Cold-Flow PSE Solution With Mach Numbers Between 5 And 14.

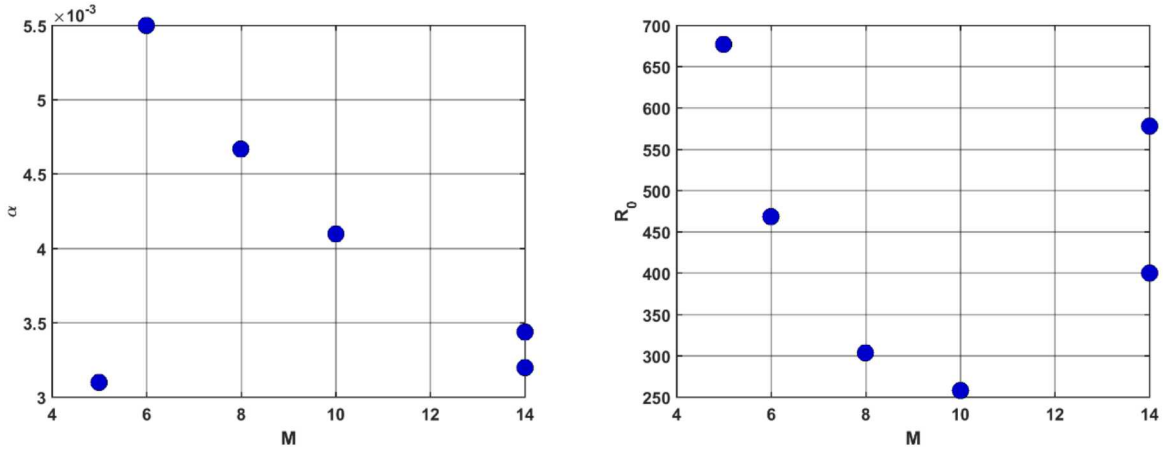

(a) Growth rate $\alpha(dN/dR)$ as a function of the Mach number

(b) Stability Reynolds number at neutral point

Figure 2-4: Effect M_∞ on α and R_0 for Cold-Flow PSE solutions at M = 5, 6, 8, 10 and 14.

2.4 COMPILATION AND ANALYSIS OF SECOND-MODE AMPLITUDES

2.4.1 Methodology

This section compiles and analyzes second-mode amplitudes obtained from surface pressure fluctuation measurements from PCB-132 pressure sensors. The second-mode amplitudes at each PCB sensor location are computed by integrating the power spectral density (PSD) over the second-mode peak. The steepness of the PSD near the second-mode peak implies that the most of the energy is located near the peak and that variations in bounds of integration have a small effect on the computed amplitudes. The PSD are calculated using Welch's method using Hanning windows with 50 percent overlap and a fast Fourier transform (FFT) length of 4,096 points. To compare the amplitudes at different unit Reynolds numbers (and freestream pressures), the amplitudes are normalized by the static pressure at the cone surface. In this study, the cone pressures are obtained by using the Taylor-Maccoll conical-flow solution.

The analysis of the second-mode amplitudes follows the methodology from Marineau et al. [10]. As previously mentioned, the sharp cone N factors from PSE can be expressed as a linear function of R. Prior to the start of transition (in the linear regime), the second mode amplitude A exhibits an exponential growth such that

$$A = ce^{dR}, \tag{6}$$

where c and d are constants. Fitting the measured amplitudes using Eq. 6 reveals that $d \approx \alpha$ which is not surprising because

1) Both constants correspond to the growth rate.

2) The measured and computed growth rates agree well.

In Figure 2-5, the exponential fit of the measured amplitude using Eq. 6 with $d = \alpha$ (red line) shows good agreement with the circumferentially averaged measurements (black line) for conditions C1, C2, C3, C4, and C5 corresponding to Re/m of 11.9, 7.1, 3.5, 2.1, and 1.7×10^6/m. In addition, since

$$A = A_0 e^N = A_0 e^{\alpha R + b}, \tag{7}$$

the initial amplitude can be estimated by combining Eqs. 6 and 7 as

$$A_0 = ce^{-b}. \tag{8}$$

Here, A_0 can be interpreted as a mean initial amplitude for the unstable frequencies over the range of fitted amplitudes. This is an approximation as the initial amplitudes are expected to vary as a function of frequency. However, as seen by the quality of the fits in Figure 2-5 and the results to be presented in Section 2.4.2, Eq. 6 provides a good model for the second-mode growth. Finally, Eqs. 7 and 8 estimate the experimentally measured N factors as

$$N(s) = ln(A(s)e^b/c). \tag{9}$$

The N factors determined experimentally with Eq. 9 and computed with PSE are compared in Section 2.4.4.

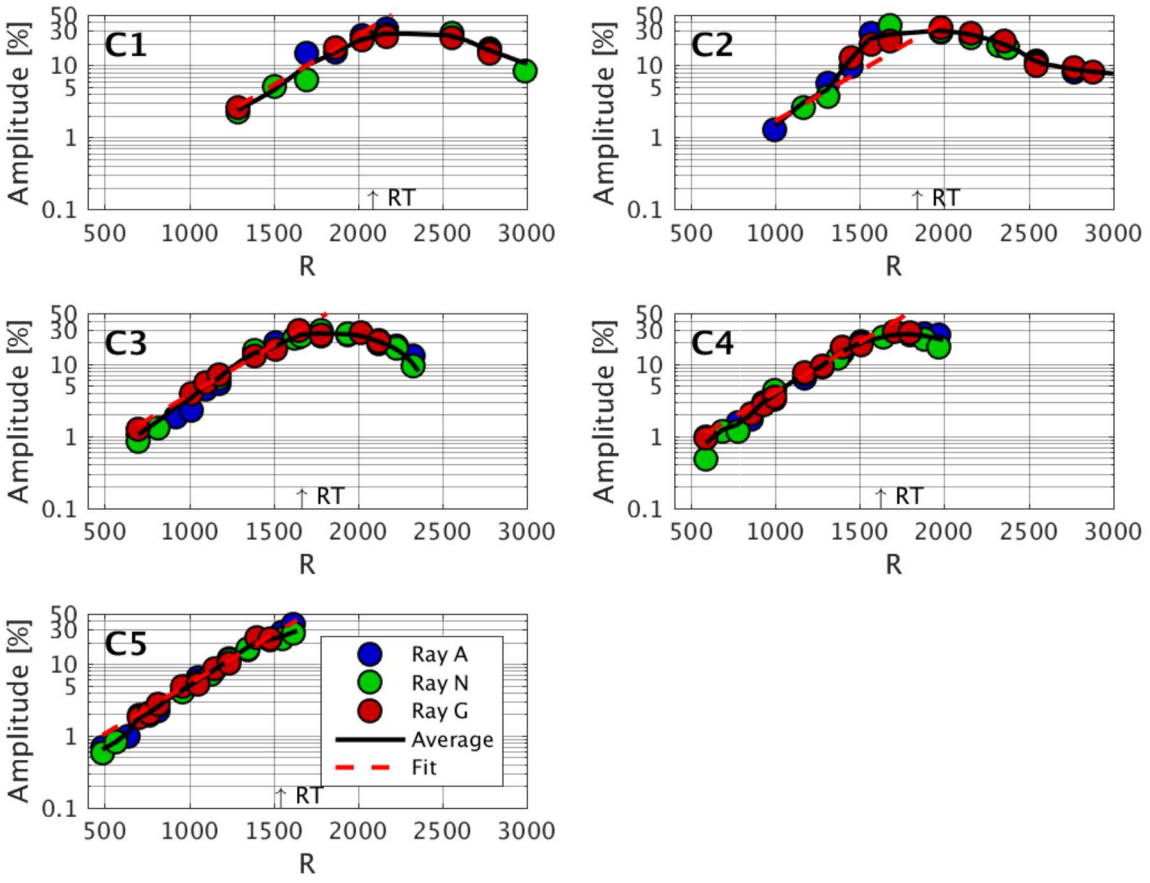

Figure 2-5: A vs. R At $M = 14$ In T9 For $Re/m = 11.9$, 7.1, 3.5, 2.5, And 1.7×10^6/m (C1 to C5), Where ↑ RT $\equiv R_T$.

2.4.2 Effect of Unit Reynolds Number, Mach Number, and Tunnel Geometry

The measured amplitudes as a function of the stability Reynolds number are plotted in Figure 2-6. The arrows indicate the start of transition in Tunnel 9 based on heat transfer measurements. The solid lines are exponential fits of the amplitude using the growth rate from the PSE solutions as described in the previous section. Figure 2-6a presents the Tunnel 9 Mach 14 data for 5 conditions corresponding to Re/m equal to 11.9, 7.1, 3.5, 2.1, and 1.7×10^6/m. The HWT-14 amplitudes at 3.3×10^6/m are also included for comparison. The Tunnel 9 data consist of circumferentially averaged amplitudes from 3 rays [10] (shown in Figure 2-5). Several important observations can be made from Figure 2-6a.

1) The second-mode saturation (maximum) amplitudes A_{max} do not vary significantly with Re/m.

2) The R location of A_{max} occurs slightly downstream of R_T.

3) The measured growth rate $\frac{dA}{dR}$ does not significantly change with Re/m.

4) The measured $\frac{dA}{dR}$ agrees with the computed growth rate α as shown by the overall quality of the curve-fits.

5) At a fixed R value, the amplitudes decrease with Re/m which combined with observations 1, 2 and 3 implies that the R_T increase with Re/m.

6) At comparable Re/m (3.3 and 3.5×10^6) the smaller HWT-14 produces amplitudes 3 to 5 times greater than the larger Tunnel 9.

Observations 3 and 4 indicate that the growth rate computed with PSE can predict the measured growth rate. Observation 5 implies that the initial amplitudes of the waves decrease with the unit Reynolds number. This is investigated further in Section 2.5. Figure 2-6b presents similar results for the Tunnel 9 data at Mach 10. VKI measurements at 6.2, 4.7 and 3.8×10^6/m are also included for comparison. As for Mach 14, the predicted growth rate matches the measurements quite well. The amplitudes measured in VKI are approximately 5 times larger than that in Tunnel 9 at similar Re/m. In addition, the saturation amplitudes measured in Tunnel 9 and VKI are similar. The maximum amplitudes A_{max} decrease with increasing Re/m. The reason for this behavior is not clear, but could be sensor related since the wavelength of the second-mode decreases with unit Re/m due to the thinner boundary-layer. This makes the measurements more susceptible to spatial averaging over the sensing element area. In addition, the frequencies increase with Re/m which makes the measurements more uncertain as the upper limit of the PCB-132 bandwidth is not precisely known and could vary among the sensors. As for Mach 14, the second-mode saturation occurs slightly downstream of the start of transition S_T. The saturation amplitudes at Mach 10 and 14 are comparable.

Figure 2-6c present amplitude measurements for the NASA 31inM10. The quality of the fit is difficult to assess due to the low number of sensors and large sensor spacing. The saturation amplitudes are comparable to that of Tunnel 9 at the same nominal Mach number. The amplitudes measured in HWT-8 are shown in Figure 2-6d. The measurements are consistent with the Mach 10 and Mach 14 measurement regarding the effect of Re/m on the amplitude of the waves and the saturation location. The saturation amplitudes, varying from 20% to 30%, are similar to the measurements at Mach 10 and 14. Therefore, it appears that the Mach number has a weak effect on the saturation amplitudes at Mach numbers between 8 and 14.

The plots in Figure 2-6e and 2-6f present Mach 6 measurements from the 20inM6 and HLB. In the HLB, the test article is positioned above the nozzle centerline to avoid the turbulence and the velocity deficit downstream of the center-body valve. The saturation amplitudes in both Mach 6 tunnels are similar at approximately 10% which is significantly lower than at the higher Mach numbers. The data at the two lowest Re/m in the 20inM6 shows good agreement with the fit. The agreement is harder to evaluate at the higher Re/m because of the low number of sensors in the region of exponential growth. For most Re/m, the amplitudes measured by the most upstream sensor are significantly lower than the fit. This might be due to the lower noise content at higher frequency, as the fit essentially assumes a constant initial amplitude. The large number of sensors and the wide range of Re/m in the HLB experiments make it possible to assess the quality of the curve-fits and the effect of Re/m on the saturation location. In general, the growth rate is well predicted by PSE. In addition, the effect of Re/m is consistent with the data at higher Mach numbers as the amplitudes decrease with Re/m at a fixed R.

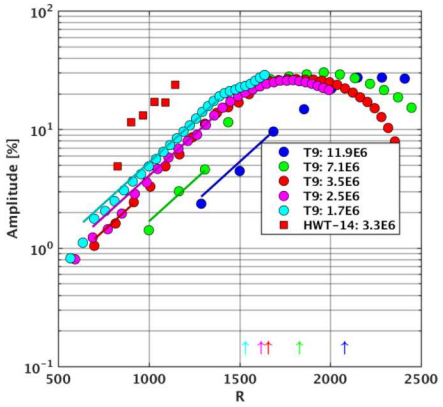

(a) Mach 14: T9 and HWT-14

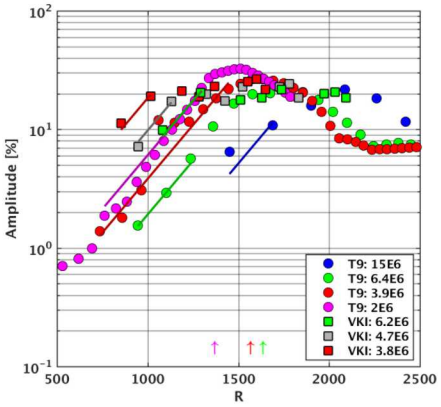

(b) Mach 10: T9 and VKI

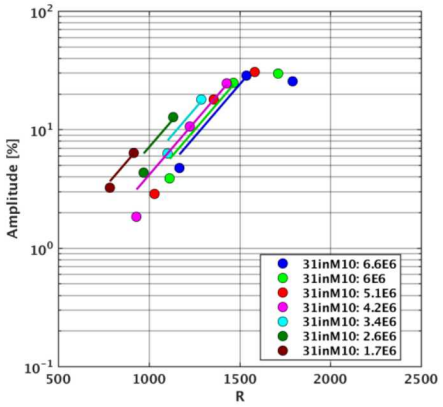

(c) Mach 10: 31inM10

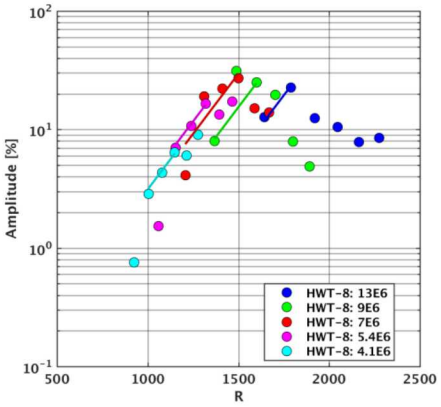

(d) Mach 8: HWT-8

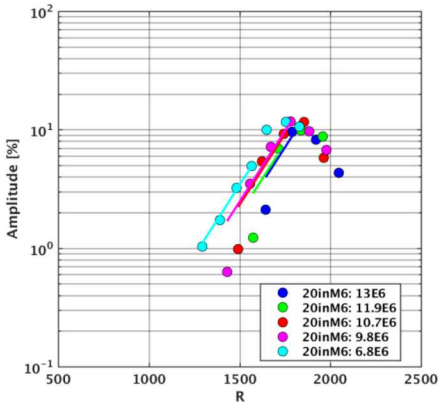

(e) Mach 6: 20inM6

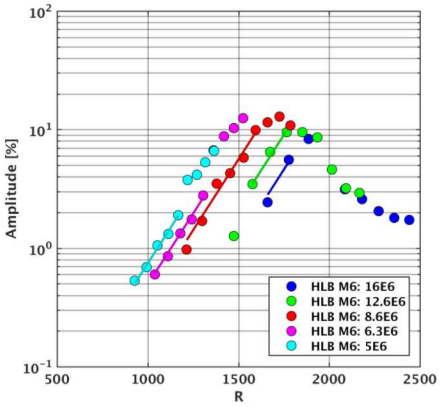

(f) Mach 6: HLB

Figure 2-6: A vs. R At $M = 6$, 8, 10, and 14 For Cold Flow Tunnels.

The second-mode amplitudes for Re/m near 6.5×10^6/m in four Mach 6 wind tunnels are shown in Figure 2-7. Data from the 20inM6, 15inM6, HLB and BAM6QT (Noisy and Quiet) are included. The dashed lines are exponential fits from Eq. (7) using the growth rate from PSE. The measured growth rates are similar in the 20inM6, 15inM6, and HLB. Since BAM6QT has only one measurement location, it is not possible to evaluate the quality of the fit for that tunnel. The amplitudes in the HLB, 15inM6, and BAM6QT (noisy) are within $\approx$ 25%, but 2 to 3 times larger than in the 20inM6. The differences could be due to the lower freestream noise content in the 20inM6 as indicated by pitot noise measurements compiled by Duan et al. [33]. This should be explored further by systematically comparing the freestream noise PSD in the different facilities. The amplitudes in BAM6QT under quiet flow are approximately 450 times smaller than under noisy flow [1].

The second-mode amplitudes in the HEG and HIEST shock tunnels are presented in Figure 2-8 for 7-deg cones with a 2.5 mm nosetip radius. The freestream Mach number and stagnation enthalpy are approximately constant at 8 and 3 MJ/kg respectively. The unit Reynolds number varying from 2.5×10^6 to 4.8×10^6/m are specified in the legend. The maximum second-mode amplitudes are between 20% and 30%, which is comparable to the values achieved for cold flow in the HWT-8. At each condition, the growth rate dA/dR appears fairly constant prior to saturation. However, the growth rates vary among the conditions. For instance, the HIEST run at Re/m = 3.3×10^6 has a much steeper slope compared to the other conditions. These variations in growth rate could be due to the effect of the nosetip bluntness. Future comparisons with PSE solutions could help better understand these variations.

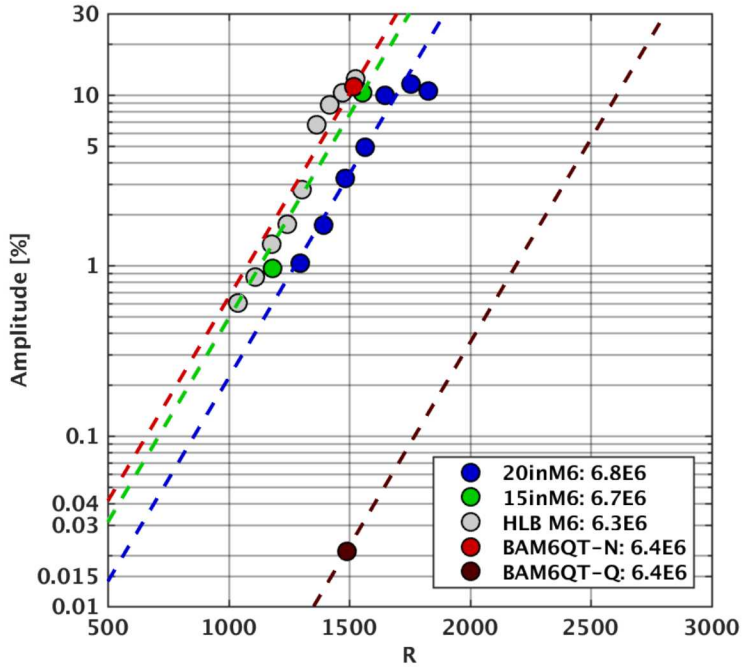

Figure 2-7: A vs. R at M =6 For $Re/m \approx 6.5\times10^6$/m.

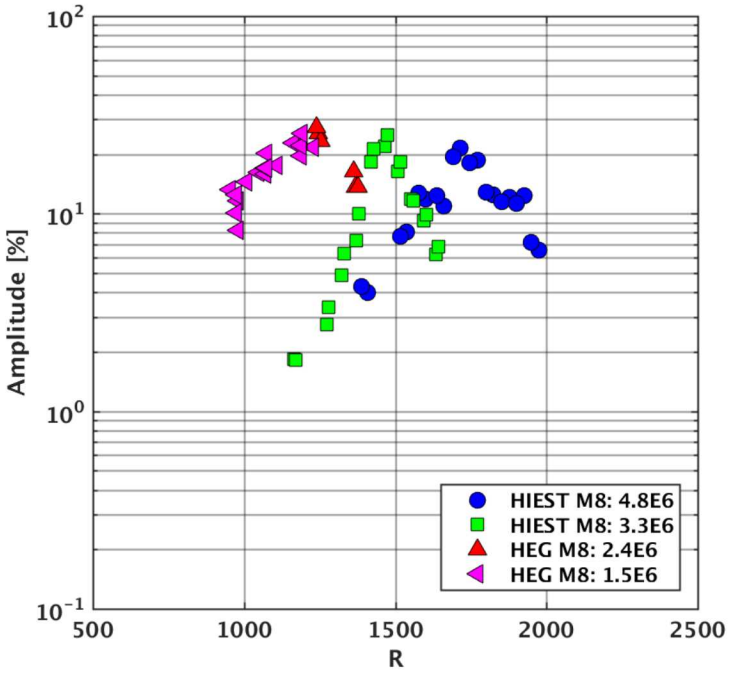

Figure 2-8: A vs. R at $M = 8$ in HIEST and HEG for $h_0 \approx 3$ MJ/kg.

2.4.3 Maximum Second-Mode Amplitudes

Marineau [15] presented a correlation for the maximum amplitudes for blunt and sharp cones at a nominal freestream Mach number of 10. The correlation included sharp cones data at nonzero AOA as well as blunt cone data with small nosetip radii at 0 deg AOA where transition still appeared to be second-mode dominated, but where the edge Mach number and breakdown amplitudes were much lower. The results from Marineau [15] were consistent with sharp cone measurements in several hypersonic wind tunnels that revealed increasing maximum amplitudes with increasing edge Mach numbers [9]. Fedorov and Kozlov [34] compiled these measurements to show a linear relationship between the edge Mach number and the maximum pressure amplitudes. The pressure amplitudes normalized by the boundary-layer edge pressure are approximately 6% at $M_e \approx 4.6$ and 24% at $M_e \approx 6.8$ which are similar to the values measured in Tunnel 9.

The maximum second-mode amplitudes compiled in this study for sharp cones at 0 deg AOA are plotted as a function of the edge Mach number in Figure 2-9. The data all are for 7-deg cones with the exception of the BAM6QT-Q (quiet) data on a flared cone ($M_e \approx 5$), and a 3-deg cone ($M_e \approx 5.8$) and the BAM6QT-N (noisy) data on a 2.5-deg cone ($M_e \approx 5.8$). For the sharp cones, M_e is obtained from the Taylor-Maccoll conical-flow solution. For the flared cone, M_e is from the mean flow CFD solution (return from enthalpy overshoot to 100.3% of the freestream total enthalpy). The data from Figure 2-9 shows a weak variation of A_{max} with M_e at $M_e >\approx 5.8$. At $M_e \approx 10$, the mean value of A_{max} ($\pm$ one standard deviation) are 27.8% $\pm$ 1.8%, compared to 26.3% $\pm$ 4.1% at $M_e \approx 8$ and 23.6% $\pm$ 4.5% for M_e between 6 and 7. The sharp decrease of A_{max} for M_e less than 5.8 is consistent with the results presented by Marineau [15] on blunt cones at a nominal freestream Mach number of 10. The values of A_{max} from HLB and 20inM6 are consistent. The mean value of A_{max} at $M_e \approx 5.3$ is 11%

$\pm$ 1.8%. The values obtained in the BAM6QT under quiet flow are higher than the values under noisy flow at a similar edge Mach number. This seems to indicate that the tunnel noise decreases the maximum second-mode amplitudes. The effect of tunnel noise on A_{max} warrants further investigation.

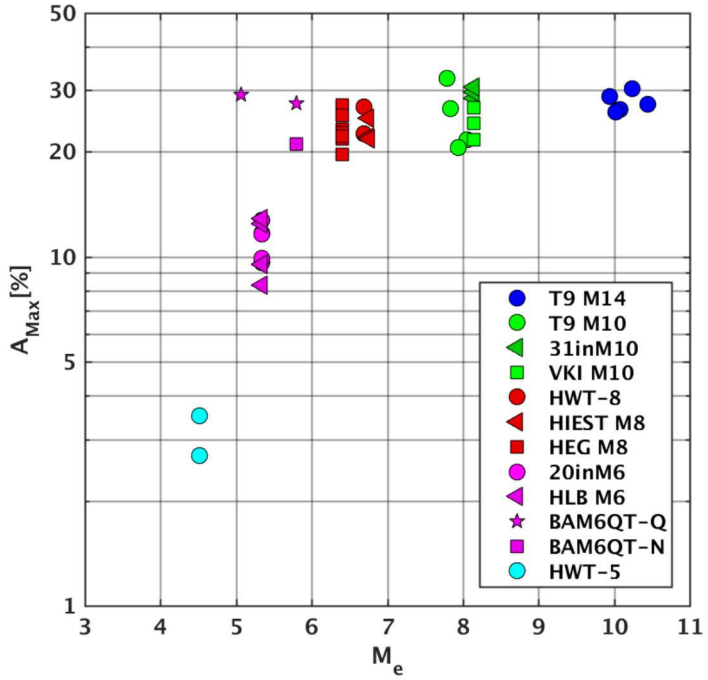

Figure 2-9: A_{max} vs. M_e.

2.4.4 Scaling of the Second-Mode Amplitudes and Comparison with Linear Stability

The measured amplitudes are normalized using the methodology presented in Section 2.4.1. Using Eq. 9, the measured amplitude can be expressed as N factors. The measured and computed N factors are compared in Figure 2-10. The arrows indicate the start of transition in Tunnel 9 based on heat transfer measurements. Figure 2-10a presents the Tunnel 9 Mach 14 data for 5 conditions with Re/m equal to 11.9, 7.1, 3.5, 2.1, and 1.7×10^6/m. The HWT-14 data at 3.3×10^6/m are also included. Good agreement with PSE and low experimental scatter are found. Over all the conditions, the computed and measured N factors are within $\pm$0.5 with the exception of the 7.1×10^6/m condition near the start of transition (within $\pm$1). An inspection of the PSD for this condition revealed an anomaly near 300 kHz where the amplitudes appear to be artificially amplified [10]. The experimental N factors at Mach 10 for Tunnel 9, VKI and 31inM10 shown in Figure 2-10b and 2-10c also agree with PSE. The wide range of Re/m between 2.0 and 15×10^6/m makes apparent the increase of N_T (experimental and computed) with Re/m. This behavior is consistent with Marineau [15]. The smaller VKI tunnel produces lower N_T compared to Tunnel 9. The increase of N_T with Re/m is also visible at Mach 8 in Figure 2-10d and Mach 6 in Figure 2-10e and 2-10f. In addition, the decreased growth rates with increasing freestream Mach numbers are correctly predicted with PSE as supported by the slope dN/dR for each Mach number.

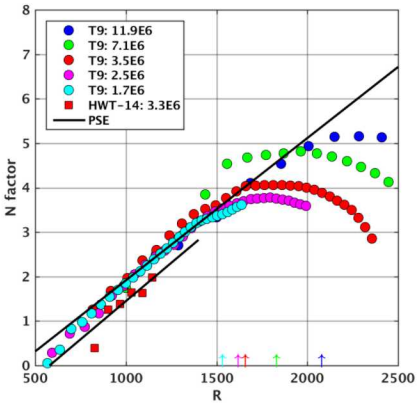

(a) Mach 14: T9 and HWT-14

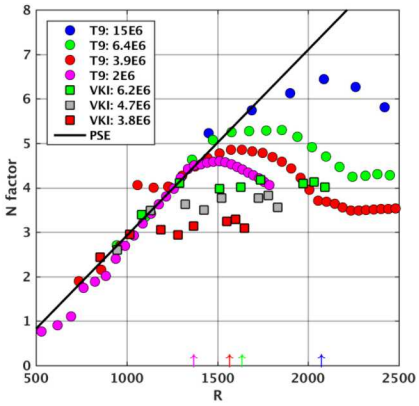

(b) Mach 10: T9 and VKI

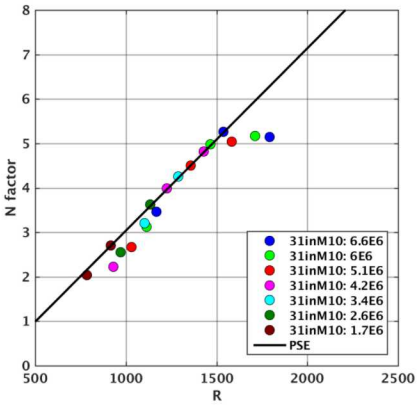

(c) Mach 10: 31inM10

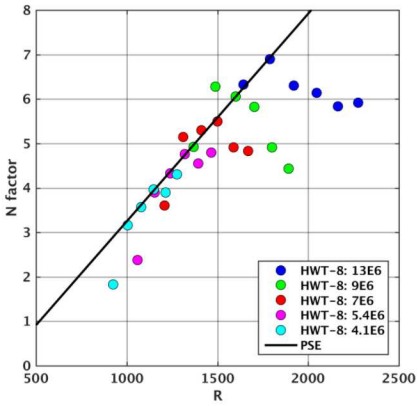

(d) Mach 8: HWT-8

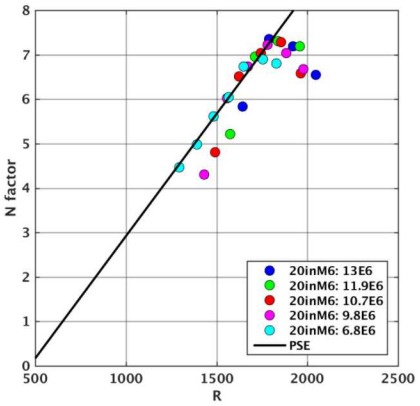

(e) Mach 6: 20inM6

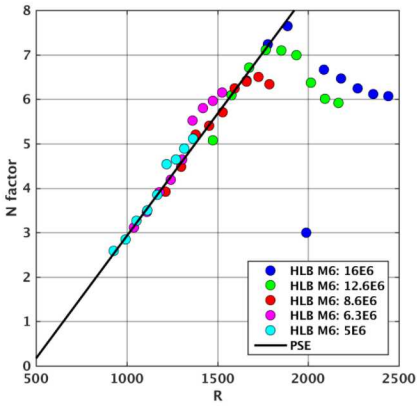

(f) Mach 6: HLB

Figure 2-10: N vs. R At $M = 6$, 8, 10, and 14 For Cold-Flow Tunnels.

2.5 SCALING OF INITIAL AMPLITUDES AND AMPLITUDE CORRELATION

2.5.1 Scaling of Initial Amplitudes with Unit Reynolds Number

This section explores the effect of Re/m on A_0. The objective is to provide a simple scaling for the variation of A_0 with Re/m for a fixed tunnel geometry and fixed Mach number. The analysis takes into account the variation of the freestream noise content with Re/m and the effect of Re/m on the unstable second-mode frequencies. We assume that the PSD of the freestream noise ϕ has a constant negative spectral slope equal to $-m$ (where m is positive) over the frequency range of interest. This assumption is reasonable based on fluctuating pitot-pressure measurements from multiple facilities [33]. Using the outer scaling [35] to account for the effect of Re/m on the PSD, we get

$$\phi_{os} = l f_{os}^{-m}, \tag{10}$$

where

$$\phi_{os} = \frac{\phi u_\infty}{p_\infty^2 \delta_n}, \tag{11}$$

and

$$f_{os} = \frac{f \delta_n}{u_\infty}. \tag{12}$$

Next, we define the freestream noise amplitude integrated over the second-mode bandwidth as

$$\Gamma_0 = \gamma_0 \sqrt{\Delta f}, \tag{13}$$

where spectral amplitudes are

$$\gamma_0 = \sqrt{\frac{\phi_0}{p_\infty^2}}. \tag{14}$$

The second-mode bandwidth is assumed proportional to the frequency as in [15] such that

$$\Delta f = w f_0, \tag{15}$$

where w is a constant. The initial amplitude can be related to the freestream noise content using the receptivity coefficient as

$$A_0 = C_R \Gamma_0. \tag{16}$$

Substituting Eqs. 10 to 15 into Eq. 16 yields

$$A_0 = C_R \sqrt{wl} \left(\frac{f_0 \delta_n}{u_\infty} \right)^{\frac{1-m}{2}}, \tag{17}$$

where f_0 is the unstable second-mode frequency corresponding initial amplitude. Because the spectral amplitudes of freestream noise decrease with frequency, A_0 decreases when f_0 increases. In Section 2.4.1, A_0 obtained in the curve-fit was interpreted as a mean initial amplitude over a range of unstable frequencies upstream of the transition location. These unstable frequencies will increase with unit Reynolds number due to the thinner boundary-layer. This effect can be accounted for by substituting the dimensionless frequency F_0 (see Eq. 1) into Eq. 17. This substitution yields

$$A_0 = C_R \sqrt{wl} \left(\frac{F_0 \delta_n Re/m}{2\pi} \right)^{\frac{1-m}{2}}. \tag{18}$$

The frequency F_0 can be evaluated at the neutral point R_0 by substituting Eq. 4 into 5. Substituting the result into Eq. 18 yields

$$A_0 = C_R\sqrt{wl}\left(\frac{g\alpha^h\delta_n Re/m}{-2\pi b^h}\right)^{\frac{1-m}{2}}. \tag{19}$$

For a fixed Mach number and tunnel geometry, all the parameters in Eq. 19 are constant with the exception of δ_n and Re/m. This also assumes that the receptivity coefficient is not a function of Re/m. This assumption is reasonable based on recent DNS studies by Balakumar and Chou [28]. Since the boundary-layer on the nozzle wall is turbulent, we can use the usual scaling for turbulent boundary layers [36] to account for the effect of Re/m on δ_n. This scaling takes the form

$$\frac{\delta_n}{L_n} \sim (Re/mL_n)^{-1/5}, \tag{20}$$

where L_n is the nozzle length. Substitution of Eq. 20 into Eq. 19 gives

$$A_0 \sim (Re/mL_n)^{\frac{4}{5}(\frac{1-m}{2})}. \tag{21}$$

Pitot noise measurements in multiple facilities [33] have shown that m =3.5 is a reasonable approximation for the spectral slope. Substituting this value into Eq. 21 yields

$$A_0 \sim (Re/mL_n)^{-1}. \tag{22}$$

Eq. 22 provides a simple relationship between A_0 and Re/m for fixed tunnel dimensions and Mach number. The validity of this expression will be evaluated in the next section.

2.5.2 Compilation of Initial Amplitudes

The initial amplitudes can be estimated from the measured amplitudes and PSE using Eq. 8. Figure 2-11 presents A_0 as a function of Re/m for Tunnel 9 at Mach 10 and 14, 31inM10, 20inM6, and HLB. Curve-fits based on Eq. 22 are also shown. Larger initial amplitudes are found in Tunnel 9 at Mach 14 compared to Mach 10. The larger initial amplitudes at Mach 14 are most likely due to the stronger tunnel noise at the higher Mach number. The initial amplitudes in the smaller 31inM10 tunnel are slightly larger than in Tunnel 9. This is consistent with the analysis of Marineau [15] based on linear stability theory and Pate's correlation [37]. Both Mach 6 tunnels have much lower amplitudes than the higher Mach number tunnels despite their smaller dimensions. This is consistent with a decrease in tunnel noise with decreasing Mach number. A decrease of the receptivity coefficient C_R with Mach number could also contribute. For unit Reynolds numbers smaller than approximately 10×10^6/m, the initial amplitude in HLB are approximately twice as large as in 20inM6. These results are consistent with the Pitot noise measurements compiled in Duan et al. [33] which showed lower tunnel noise levels in 20inM6. The curve-fits agree well with the Mach 6 data with the exception of the two HLB data points at $Re/m > 10\times10^6$/m. It would be useful to investigate if this behavior is related to an unexpected decrease in tunnel noise in HLB at $Re/m > 10\times10^6$/m.

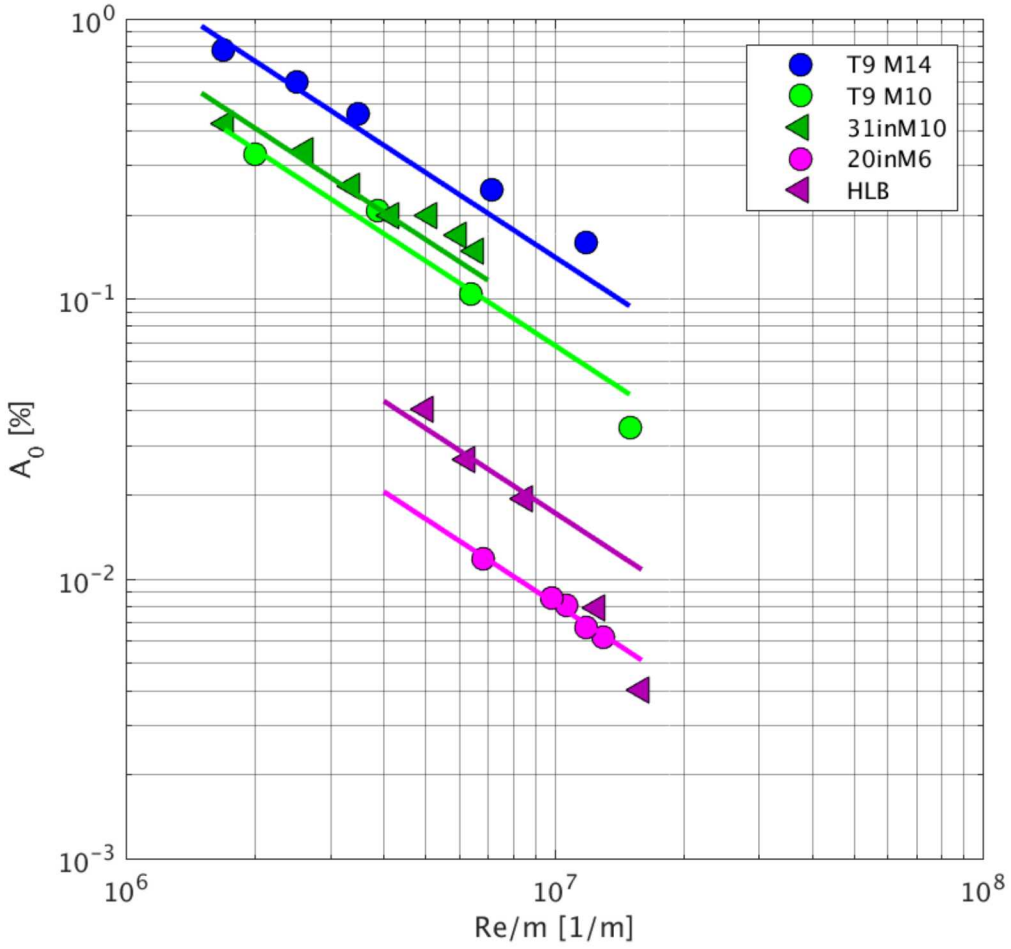

Figure 2-11: A_0 vs. Re/m. Solid Lines Are Fit For Eq. 22, $A_0 \sim Re/m^{-1.}$

2.5.3 Correlation of Second-Mode Amplitudes

In this section, the second-mode amplitudes are estimated using the N factors computed with PSE and the curve-fits for the initial amplitudes obtained in Section 2.5.2. This allows the computation of the second-mode amplitudes using Eq. 8. Figure 2-12 compares the measured amplitudes with the amplitude computed using Eq. 8. Reasonable agreement is obtained between the measured and estimated amplitudes. This implies that PSE can predict the growth of the waves and that the initial amplitudes can be estimate using curve-fits based on Eq. 22. For amplitudes greater than 4% and below the saturation, the standard error between the measurements and correlation is approximately 25%. This is reasonably good considering the simple relationship ($A_0 \sim Re/m^{-1}$) between the initial amplitudes and the unit Reynolds number. Considering that the amplitudes grow exponentially, much smaller errors ~10% are to be expected when using this methodology to estimate N_T or S_T. In addition, it is likely that improvements could be made by relating the initial amplitude to the measured freestream noise content in each facility as in [15].

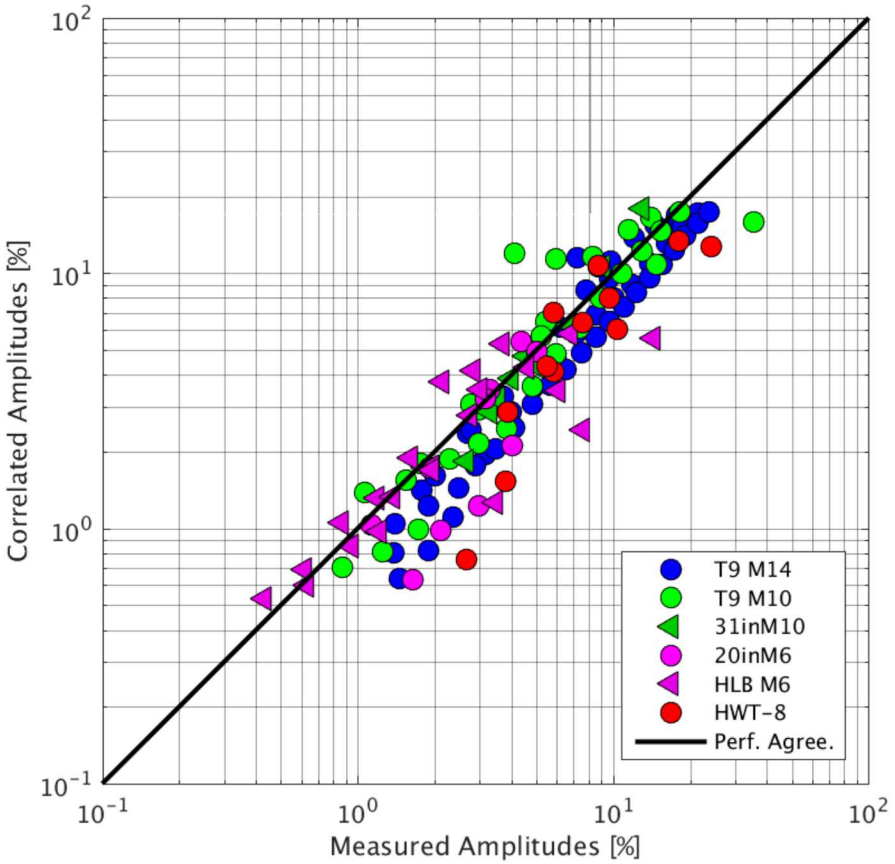

Figure 2-12: Comparison Between The Measurements And The Amplitudes Computed Using Eq. 8.

2.6 CONCLUSIONS AND FUTURE WORK

The main objectives of this international research effort coordinated by the NATO STO AVT-240 specialists' group were to compile and analyze second-mode amplitudes measured on sharp slender cones. The data were from 11 hypersonic wind tunnels from 9 organizations located in 3 NATO countries (Belgium, Germany, and USA) and Japan. These tunnels provided second-mode amplitude measurements at Mach numbers between 5 and 14, unit Reynolds numbers Re/m between 1.5 and 16×10^6/m, and wall-to-total temperature ratios T_w/T_0 between 0.1 and 0.8. The study showed that the measured second-mode growth rates can be predicted with PSE over a wide range of hypersonic conditions. PSE and measurements both showed decreasing growth rates with increasing Mach numbers greater than 6. The maximum second-mode amplitudes were found to vary weakly (from $\sim$20 to 30%) for M_e greater than approximately 5.8, but to significantly decrease at lower M_e. The maximum N factor envelope from PSE and the measured amplitudes were used to estimate the initial amplitudes A_0. At each Mach number, A_0 approximately scales as Re/m^{-1}. This leads to an increase in the transition N factors with Re/m which is consistent with the findings from Marineau [15]. As Re/m increases, the unstable second-mode frequencies also increase such that the tunnel noise spectral amplitudes are lower over that range of unstable frequencies. This explains the decrease of A_0 with Re/m.

The effect of tunnel size was explored by plotting the second-mode amplitudes from multiple facilities producing the same nominal freestream Mach number. Data from multiple cold flow wind tunnels were available at Mach 14 (HWT-14 and T9), Mach 10 (VKI, 31inM10, and T9), and Mach 6 (BAM6QT, 15inM6, HLB and 20inM6). The analysis showed that the second-mode amplitudes at similar Re/m and R decrease with increasing tunnel dimensions. This is likely because the smaller tunnels have a thinner boundary layer that produces more acoustic noise over the range of unstable second-mode frequencies. Overall, the results indicate that amplitude-based methods for hypersonic BLT predictions [15, 28] should be applicable across a wide range of hypersonic conditions, as clear and potentially universal trends were found for the effect of Re/m and tunnel sizes across the wide range of conditions. Such physics based methods are preferable to purely empirical methods such as Pate's correlation [38], as they are applicable to arbitrary geometries and are likely to provide a viable path in using ground-test data for flight prediction.

Future research will include a comparison of Mach 10 data from T9, 31inM10, and VKI with new data from LENS I at the same nominal Mach number. The LENS I study will involve similar instrumentation density and test conditions as the Tunnel 9 experiments. The effect of tunnel size and nozzle geometry (2D vs. axisymmetric) on the second-mode amplitudes also needs to be investigated in more detail.

2.6.1 Acknowledgments

Eric Marineau would like to acknowledge the Test Resource Management Center T&E / S&T HSST program for their funding as part of the Center of Testing Excellence. The authors would like to acknowledge Shann Rufer and Dennis Berridge for helping interpreting previously published data from the NASA Langley hypersonic wind tunnels. Sandia National Laboratories is a multi-mission laboratory managed and operated by National Technology and Engineering Solutions of Sandia, LLC., a wholly owned subsidiary of Honeywell International, Inc., for the U.S. Department of Energy's National Nuclear Security Administration under contract DE-NA0003525.

2.7 REFERENCES

[1] Estorf, E., Radespiel, R., Schneider, S., Johnson, H., and Hein, S., "Surface-Pressure Measurements of Second-Mode Instability in Quiet Hypersonic Flow," *AIAA Paper 2008-1153*, January 2008.

[2] Berridge, D., Casper, K., Rufer, S., Alba, C., Lewis, D., Beresh, S., and Schneider, S., "Measurements and Computations of Second-Mode Instability Waves in Several Hypersonic Wind Tunnels," *AIAA Paper 2010-5002*, June-July 2010.

[3] Rufer, S. and Berridge, D., "Experimental Study of Second-Mode Instabilities on a 7-Degree Cone at Mach 6," *AIAA Paper 2011-3877*, June 2011.

[4] Grossir, G., Pinna, F., Bonucci, G., Regert, T., Rambaud, P., and Chazot, O., "Hypersonic Boundary Layer Transition on a 7 Degree Half-Angle Cone at Mach 10," *AIAA Paper 2014-2779*, June 2014.

[5] Marineau, E., Moraru, C., Lewis, D., Norris, J., Lafferty, J., Wagnild, R., and Smith, J., "Mach 10 Boundary-Layer Transition Experiments on Sharp and Blunted Cones," *AIAA Paper 2014-3108*, June 2014.

[6] Marineau, E., Moraru, C., Lewis, D., Norris, J., Lafferty, J., and Johnson, H., "Investigation of Mach 10 Boundary Layer Stability of Sharp Cones at Angle-of-Attack, Part 1: Experiments," *AIAA Paper 2015-1737*, January 2015.

[7] Wagner, A., Kuhn, M., Schramm, J.M., and Hannemann, K., "Experiments on Passive Hypersonic Boundary Layer Control Using Ultrasonically Absorptive Carbon-Carbon Material with Random Microstructure," *Experiments in Fluidsl*, Vol. 54, No. 10, October 2013, pp. 1–10.

[8] Tanno, H., Komuro, T., Sato, K., Itoh, K., Takahashi, M., and Fujii, K., "Measurement of Hypersonic High-Enthalpy Boundary Layer Transition on a 7° Cone Model," *AIAA Paper 2010-0310*, January 2010.

[9] Casper, K., Beresh, S., Henfling, J., Spillers, R., Pruett, B., and Schneider, S., "Hypersonic Wind-Tunnel Measurements of Boundary-Layer Transition on a Slender Cone," *AIAA Journal*, Vol. 54, No. 4, January 2016, pp. 1250–1263.

[10] Marineau, E., Moraru, C., and Daniel, D., "Sharp Cone Boundary-Layer Transition and Stability at Mach 14," *AIAA Paper 2017-0766*, January 2017.

[11] Bounitch, A., Lewis, D., and Lafferty, J., "Improved Measurements of "Tunnel Noise" Pressure Fluctuations in the AEDC Hypervelocity Wind Tunnel No 9," *AIAA Paper 2011-1200*, January 2011.

[12] Rufer, S. and Berridge, D., "Pressure Fluctuation Measurements in the NASA Langley 20-Inch Mach 6 Wind Tunnel," *AIAA Paper 2012-3262*, June 2012.

[13] Schilden, T., Schröder, W., Ali, S., Schreyer, A., Wu, J., and Rodespiel, R., "Analysis of Acoustic and Entropy Disturbances in a Hypersonic Wind Tunnel," *Physics of Fluids*, Vol. 28, No. 5, May 2016, pp. 056104.

[14] Johnson, H. and Candler, G., "Hypersonic Boundary Layer Stability Analysis Using PSE-Chem," *AIAA Paper 2005-5023*, June 2005.

[15] Marineau, E., "Prediction Methodology for Second-Mode-Dominated Boundary-Layer Transition in Wind Tunnels," *AIAA Journal*, Vol. 55, No. 2, 2017, pp. 484–499.

[16] Mack, L., "Transition and Laminar Instability," *NASA-CP-153203, Jet Propulsion Lab, Pasadena, California*, 1977.

[17] Beresh, S., Casper, K., Wagner, J., Henfling, J., Spillers, R., and Pruett, B., "Modernization of Sandia's Hypersonic Wind Tunnel," *AIAA Paper 2015-1338*, January 2015.

[18] Schneider, S., "Fabrication and Testing of the Purdue Mach-6 Quiet-Flow Ludwieg Tube," *AIAA Paper 2000-0295*, January 2000.

[19] Berger, K., Rufer, S., Hollingsworth, K., and Wright, S., "NASA Langley Aerothermodynamics Laboratory: Hypersonic Testing Capabilities," *AIAA Paper 2015-1337*, January 2015.

[20] Estorf, M., Wolf, T., and Radespiel, R., "Experimental and Numerical Investigations on the Operation of the Hypersonic Ludwieg Tube Braunschweig," *In Proceedings 5th European Symposium on Aerothermodynamics for Space Vehicles, ESA SP-563*, 2005.

[21] Hannemann, K., Schramm, J.M., and Karl, S., "Recent Extensions to the High Enthalpy Shock Tunnel Göttingen (HEG)," *2nd International ARA Days, Arcachon, France*, 2008.

[22] Itoh, K., *Advanced Hypersonic Test Facilities*, chap. Characteristics of the HIEST and its Applicability for Hypersonic Aerothermodynamic and Scramjet Research, American Institute of Aeronautics and Astronautics, 2002, pp. 239–253.

[23] Grossir, G., Masutti, D., and Chazot, O., "FLow Characterization and Boundary Layer Transition Studies in VKI Hypersonic Facilities," *AIAA Paper 2015-0578*, January 2015.

[24] Holden, M., "Recent Advances in Hypersonic Test Facilities and Experimental Research," *AIAA Paper 1993-5005*, November-December 1993.

[25] Holden, M., Wadhams, T., Maclean, M., Dufrene, A., Mundy, E., and Marineau, E., "Review of Basic Research and Development Programs Conducted in the LENS Facilities in Hypersonic Flows," *AIAA Paper 2012-0469*, January 2012.

[26] Lafferty, J., Coblish, J., Marineau, E., Norris, J., Kurits, I., Lewis, D.R., Smith, M., and Marana, M., "The Hypervelocity Wind Tunnel No. 9; Continued Excellence Through Improvement and Modernization," *AIAA Paper 2015-1340*, January 2015.

[27] Marren, D. and Lafferty, J., *Advanced Hypersonic Test Facilities*, chap. The AEDC Hypervelocity Wind Tunnel 9, American Institute of Aeronautics and Astronautics, 2002, pp. 467–477.

[28] Balakumar, P. and Chou, A., "Transition Prediction in Hypersonic Boundary Layers Using Receptivity and Freestream Spectra," *AIAA Journal*, Vol. 56, No. 1, September 2017, pp. 193–208.

[29] Casper, K., Beresh, S., Henfling, J., Spillers, R., Pruett, B., and Schneider, S., "Hypersonic Wind-Tunnel Measurements of Boundary-Layer Pressure Fluctuations," *AIAA Paper 2009-4054*, June 2009.

[30] Stetson, K., Thompson, E., Donaldson, J., and Siler, L., "Laminar Boundary Layer Stability Experiments on a Cone at Mach 8, Part 1: Sharp Cone," *AIAA Paper 1983-1761*, July 1983.

[31] Bitter, N. and Shepherd, J., "Stability of Highly Cooled Hypervelocity Boundary Layers," *Journal of Fluid Mechanics*, Vol. 778, September 2015, pp. 586–620.

[32] Mack, L., "Boundary-Layer Linear Stability Theory," *AGARD Report No. 709*, North Atlantic Treaty Organization 1984.

[33] Duan, L., Choudhari, M., Chou, A., Munoz, F., Ali, S., Radespiel, R., Schilden, T., Schröder, W., Marineau, E., Casper, K., Chaudhry, R., Candler, G., Gray, K., Sweeney, C., and Schneider, S., "Characterization of Freestream Disturbances in Conventional Hypersonic Wind Tunnels," *AIAA Paper 2018-0347*, January 2018.

[34] Federov, A. and Kozlov, K., "Receptivity of High-Speed Boundary Layer to Solid Particulates," *AIAA Paper 2011-3925*, June 2011.

[35] Beresh, S., Henfling, J., Spillers, R., and Pruett, B., "Fluctuating Wall Pressures Measured Beneath a Supersonic Turbulent Boundary Layer," *Physics of Fluids*, Vol. 23, No. 7, July 2011, pp. 075–110.

[36] Smits, A. and Dussauge, J.P., *Turbulent Shear Layers in Supersonic Flow*, Springer, 2nd ed., 2006, p. 213.

[37] Pate, S., "Dominance of Radiated Aerodynamic Noise on Boundary-Layer Transition in Supersonic/Hypersonic Wind Tunnels," *AEDC-TR-77-107*, 1978.